Topological transitions and topological beam splitters in gyromagnetic metamaterials

Mingzhu Li [1], Ning Han [2,3,*] Lu Qi [4] Yu Yan [5] Rui Zhao [5] and Shutian Liu [5,†]

[1] *School of Information and Electrical Engineering, Hangzhou City University, Hangzhou 310015, China*
[2] *Interdisciplinary Center for Quantum Information, State Key Laboratory of Modern Optical Instrumentation, College of Information Science and Electronic Engineering, Zhejiang University, Hangzhou 310027, China*
[3] *ZJU-Hangzhou Global Science and Technology Innovation Center, Key Laboratory of Advanced Micro/Nano Electronic Devices and Smart Systems of Zhejiang, ZJU-UIUC Institute, Zhejiang University, Hangzhou 310027, China*
[4] *School of Physical Science and Technology, Yangzhou University, Yangzhou 225002, China*
[5] *School of Physics, Harbin Institute of Technology, Harbin 150001, China*

(Received 28 July 2023; revised 20 January 2024; accepted 7 February 2024; published 23 February 2024)

Topological transitions unveil a fundamentally novel pathway of research, revealing captivating optical phenomena in electromagnetic metamaterials. In this work, we give comprehensive pictures of topological phase diagrams and topological transitions in the gyromagnetic metamaterials (GMs). We comprehensively demonstrate the topology of all types of equifrequency surfaces of the GMs. The Weyl points and the nodal line can coexist in the GMs, and they are the critical points in the topological transitions. The localized Fermi arc surface states exist at the boundary between the vacuum state and GMs owing to the bulk-edge correspondence of the material system. Full-wave simulations reveal that topological surface waves can smoothly transmit forward around the square defect without reflection or scattering. Remarkably, different types of topological beam splitters are demonstrated utilizing the topological surface waves in the GMs. We theoretically demonstrate that the physical mechanism of achieving the topological beam splitters is caused by different group velocity directions of the Fermi arcs surface states of the material system. Moreover, the topological wave division and controllable propagation of the Fermi arc surface states can be achieved by adopting the different boundary configurations and gyromagnetic parameters in the topological beam splitters. Our work could broaden insights into topological wave physics and provide more flexibility for photonic devices in the electromagnetic media.

DOI: 10.1103/PhysRevB.109.085429

I. INTRODUCTION

The topological phases of matter are protected by the global characteristics of the band structure and have robustness to the local perturbations (defects) [1–7]. Topological phases possess nontrivial chiral edge states at the boundary because of the bulk-edge correspondence [8–10]. The research on topological phases in photonic systems originated from solid-state materials, and then a lot of new topological phases have been found and demonstrated experimentally, such as the topological Chern vector [11], chiral zero mode [12,13], and skyrmion surface state [14]. In particular, the topological semimetals possess three different types due to the dimensionality of the band structure degeneracies: zero-dimensional (0D) Dirac and Weyl semimetals [15–19], one-dimensional (1D) nodal line (chain/ring) semimetals [20–23], and two-dimensional (2D) nodal surface semimetals [24,25]. Recently, the photonic topological semimetals have become a hot topic because of their fascinating application prospects, including topological negative refraction [26,27], copropagating Fermi arc surface states [28,29], and topological switches [30]. Moreover, the nodal line (surface) semimetals can transform into the Dirac semimetals and Weyl semimetals when symmetry-lowering mechanisms (such as spin-orbit coupling) are introduced into the system [31,32].

In photonic systems, the transmission of light in bulk materials can be described by the equifrequency surface. It is similar to the Fermi surface of electrons in the crystal structures [33]. Different from the conventional ellipsoidal and spherical shaped equifrequency surfaces studied in the natural medium, the hyperbolic equifrequency surfaces of singular types can be found in metamaterials [34–37]. Particularly, the hyperbolic equifrequency surfaces have distinct dispersion features that are unattainable in the conventional ellipsoidal and spherical equifrequency surfaces. The hyperbolic equifrequency surfaces have demonstrated several unusual features, including subwavelength imaging, negative refraction, and spontaneous emission [34,36]. On the other hand, different forms of equifrequency surfaces have dissimilar topological characteristics. A new method to control light-matter interactions can be achieved by altering the topology of equifrequency surfaces in electromagnetic metamaterials [34]. In general, the ellipsoidal and spherical closed-shape equifrequency surfaces cannot be smoothly transformed into the hyperbolic open-shape equifrequency surfaces; i.e., the topological transitions occur during this change process [34,36].

*ning_han@zju.edu.cn
†stliu@hit.edu.cn

In recent years, the topological beam splitters based on the topological edge states in the phononic crystals and photonic crystals have been proposed and studied [38–41]. Based on the topological beam splitting effect, some interesting applications can be achieved in the topological phononic crystals and photonic crystals, such as on-chip valley-dependent quantum information [38], the topological valley Hall effect [40], and temporal beam splitters [41]. However, phononic crystals and photonic crystals generally rely on complex structures and carefully designed geometric dimensions. By contrast, gyromagnetic metamaterials (GMs) are kinds of electromagnetic metamaterials [42–45]. They are homogeneous continuum media and the electromagnetic response of the GMs can be described by effective electromagnetic tensors (the permittivity and permeability tensors). The GMs do not possess time-reversal symmetry owing to the magneto-optical effect under an external magnetic field. Recently, the GMs have been extensively investigated in the fields of non-Hermitian triply degenerate points [42], Weyl semimetals [43], and unidirectional disorder-immune propagation [44]. Moreover, the commonly used material is the yttrium iron garnet to realize the GMs in the experiment [44,45].

In this work, we study the topological transitions and achieve the topological beam splitters in the GMs. We analytically calculate the conditions for the critical points of topological transitions and comprehensively draw the topological phase diagrams by solving the bulk state equation of the GMs. We demonstrate that node lines and Weyl points can coexist in GMs. These nodal lines and Weyl points are the critical points in the topological transitions and possess the spatial inversion symmetry protection mechanism. The surface waves at the boundary between the vacuum state and GMs are demonstrated to propagate robustly against the multiple-step transition by the COMSOL numerical simulation. Remarkably, we can realize the topological beam splitters between the GMs and vacuum state based on the topological surface waves. We reveal that the physical mechanism of achieving the topological beam splitters is caused by the different group velocity directions of the Fermi arc surface states of the vacuum state–GMs system. Moreover, the topological beam splitters can be made direction reconfigurable by manipulating the locations of the vacuum state and GMs.

This paper is organized as follows. In Sec. II, three-dimensional (3D) band structure, the topological phase diagram, Weyl points, and nodal lines of the GMs are investigated. Topological transitions in the GMs are studied in Sec. III. The topological surface wave and topological beam splitter are shown in Sec. IV. Finally, we summarize the work and present our conclusions in Sec. V.

II. 3D BAND STRUCTURE, TOPOLOGICAL PHASE DIAGRAM, WEYL POINT, AND NODAL LINE OF THE GMs

The relative permittivity and permeability tensors of the GMs can be described as

$$\bar{\boldsymbol{\epsilon}} = \mathrm{diag}(\epsilon_t, \epsilon_t, \epsilon_z), \bar{\boldsymbol{\mu}} = \begin{pmatrix} \mu_t & ig & 0 \\ -ig & \mu_t & 0 \\ 0 & 0 & \mu_z \end{pmatrix}, \quad (1)$$

where $\epsilon_z = 1 - \omega_p^2/\omega^2$, $\mu_t = 1 + \omega_m\omega_0/(\omega_0^2 - \omega^2)$, and $g = \omega_m\omega/(\omega_0^2 - \omega^2)$. ω_p is the plasma frequency, ω represents the angular frequency, and ω_m and ω_0 are the characteristic frequency and resonance frequency [11], respectively. Moreover, ϵ_t ($\epsilon_t = 2$) and μ_z ($\mu_z = 1$) in Eq. (1) are frequency-independent constant values.

The corresponding GMs can be realized by using the periodic multilayered structure of the metal-ferrite superlattice [36]. Using layered material to construct an effective metamaterial has been widely accepted and used in the designing of electromagnetic metamaterials [46,47]. The whole system can regarded be as a single anisotropic medium when the layers are thin enough. Then, based on the effective medium theory, the effective constitutive parameters can be obtained. Particularly, the layered media and the thickness of each layer can be adjustable in a reasonable range. This gives us the freedom to realize the required electromagnetic parameters of the GMs in Fig. 1.

In the GMs, the constitutive relation is given by

$$\begin{pmatrix} \mathbf{D} \\ \mathbf{B} \end{pmatrix} = \begin{pmatrix} \bar{\boldsymbol{\epsilon}} & 0 \\ 0 & \bar{\boldsymbol{\mu}} \end{pmatrix} \begin{pmatrix} \mathbf{E} \\ \mathbf{H} \end{pmatrix}. \quad (2)$$

Combining $\nabla \times \mathbf{E} = \mathbf{i}\omega\mathbf{B}$ and $\nabla \times \mathbf{H} = -\mathbf{i}\omega\mathbf{D}$, Maxwell equations in the GMs can be recast to a 6×6 matrix form,

$$\left[\begin{pmatrix} i\bar{\boldsymbol{\kappa}} & 0 \\ 0 & i\bar{\boldsymbol{\kappa}} \end{pmatrix} - i\omega \begin{pmatrix} \bar{\boldsymbol{I}} & 0 \\ 0 & -\bar{\boldsymbol{I}} \end{pmatrix} \begin{pmatrix} 0 & \bar{\boldsymbol{\mu}} \\ \bar{\boldsymbol{\epsilon}} & 0 \end{pmatrix}\right] \begin{pmatrix} \mathbf{E} \\ \mathbf{H} \end{pmatrix} = 0, \quad (3)$$

where $\bar{\boldsymbol{I}}$ represents the identity tensor matrix and $\bar{\boldsymbol{\kappa}} = [0, -k_z, k_y; k_z, 0, -k_x; -k_y, k_x, 0]$. For simplicity, the angular frequency ω, characteristic frequency ω_m, and plasma frequency ω_p are normalized to ω_0, and the wave vector k is normalized to k_0 ($k_0 = \omega_0/c$), where c represents the speed of light in the free space. In the GMs, the wave propagation of the electric field $\mathbf{E}$ can be described as

$$[\bar{\boldsymbol{\kappa}} \cdot (\omega\bar{\boldsymbol{\mu}})^{-1} \cdot \bar{\boldsymbol{\kappa}} + \omega\bar{\boldsymbol{\epsilon}}]\mathbf{E} = 0. \quad (4)$$

Equation (4) represents the master equation of the GMs and can be specifically written in the component form

$$\begin{pmatrix} -\frac{k_z^2 a + (k_y^2 - \omega^2\epsilon_t)b}{\omega b} & \frac{k_x k_y}{\omega} + \frac{i k_z^2 \omega_m}{b} & -\frac{k_z(i\omega k_y \omega_m - k_x a)}{\omega b} \\ \frac{k_x k_y}{\omega} - \frac{i k_z^2 \omega_m}{b} & -\frac{k_z^2 a + (k_x^2 - \omega^2\epsilon_t)b}{\omega b} & -\frac{k_z(-i\omega k_x \omega_m - k_y a)}{\omega b} \\ -\frac{k_z(-i\omega k_y \omega_m - k_x a)}{\omega b} & -\frac{k_z(i\omega k_x \omega_m - k_y a)}{\omega b} & -\frac{(k_x^2 + k_y^2)a + (\omega_p^2 - \omega^2)b}{\omega b} \end{pmatrix} \begin{pmatrix} E_x \\ E_y \\ E_z \end{pmatrix} = 0, \quad (5)$$

where $a = -\omega^2 + \omega_0^2 + \omega_0\omega_m$ and $b = -\omega^2 + \omega_0^2 + 2\omega_0\omega_m + \omega_m^2$.

In the above square matrix [Eq. (5)], the existence of nontrivial solutions for electric fields $\mathbf{E}$ requires that

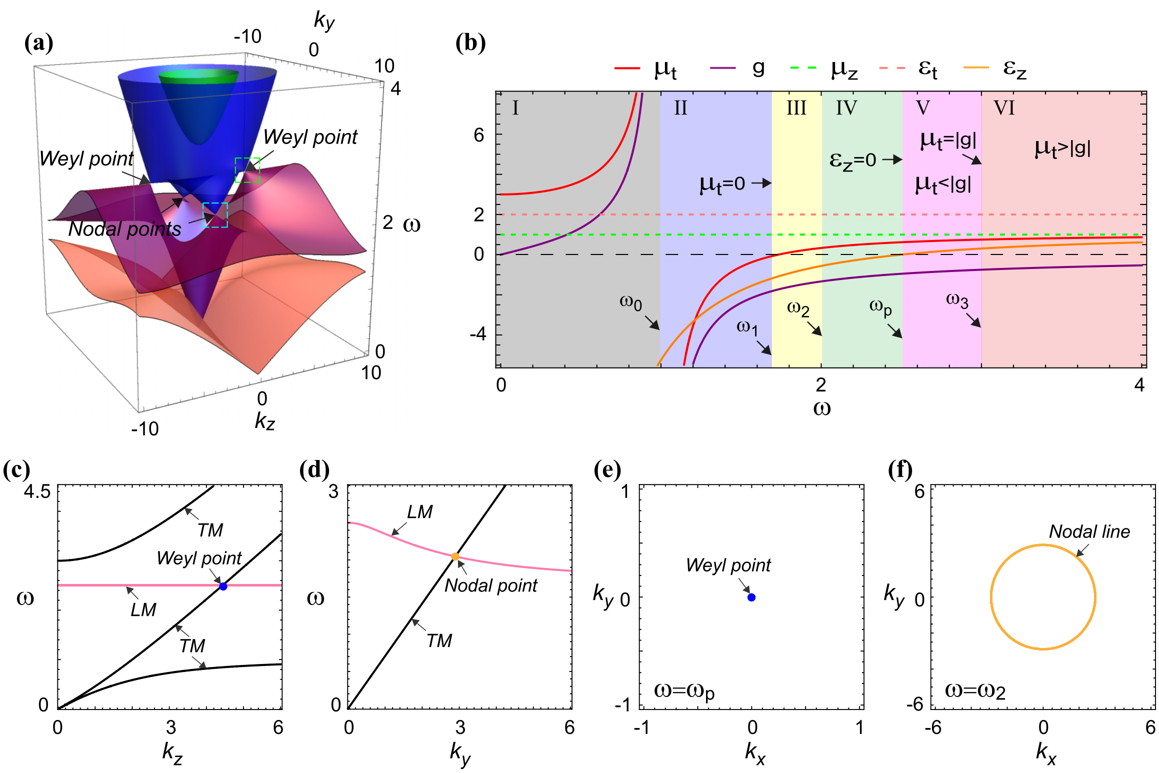

FIG. 1. 3D band structure, topological phase diagram, Weyl point, and nodal line of the GMs. (a) 3D band structures ($k_x = 0$) for GMs [based on Eq. (6)]. The green and cyan dashed boxes show Weyl points and nodal points (projection of the nodal lines), respectively. (b) The topological phase diagram in GMs where the values of μ_t, g, μ_z, ϵ_t, and ϵ_z change with the angular frequency ω. The Roman numerals I–VI represent six different topological phases. The electromagnetic parameters of the GMs are $\epsilon_t = 2$, $\omega_0 = 1$, $\omega_m = 2$, and $\omega_p = 2.5$. (c) and (d) The dispersion along the z and y directions of the GMs, respectively. The pink and black lines represent the dispersions of the LM and TM of the Weyl point and nodal line, respectively. (e) and (f) The projection of the Weyl point and nodal line in the k_x-k_y plane, respectively.

its determinant be zero. In particular, the characteristic equation of the GMs can be given by

$$\left(k_x^4 + k_y^4\right) a\omega^2\epsilon_t + d\left(\omega^2 - \omega_p^2\right) + k_x^2(e+f) - k_y^2(g+h) = 0, \tag{6}$$

where $d = -2a\omega^2 k_z^2\epsilon_t + b\omega^4\epsilon_t^2 + k_z^4(-\omega^2 + \omega_0^2)$, $e = \omega^2\epsilon_t(-b\omega^2 + 2ak_y^2 - a\omega^2\epsilon_t + b\omega_p^2)$, $f = k_z^2[\epsilon_t(-\omega^4 + \omega^2\omega_0^2) + a(\omega^2 - \omega_p^2)]$, $g = \omega^2\epsilon_t[a\omega^2\epsilon_t + b(\omega^2 - \omega_p^2)]$, and $h = k_z^2[\epsilon_t(\omega^4 - \omega^2\omega_0^2) + a(-\omega^2 + \omega_p^2)]$.

To demonstrate the existence of the Weyl point and nodal line in the GMs [Fig. 1(a)] and study their related topological characteristics, we deduced the expressions of the transverse mode (TM) and longitudinal mode (LM) that form the Weyl point and nodal line based on the eigen-electric-field of the GMs. Along the z axis ($k_x = k_y = 0$), the characteristic equation [Eq. (6)] of the GMs can be further described as

$$\omega^2 - \omega_p^2 = 0, \tag{7}$$

$$\begin{aligned}&\left(-\omega_0^2 + \omega^2\right)k_z^4 + 2\omega^2 k_z^2\epsilon_t\left(\omega_0^2 + \omega_0\omega_m - \omega^2\right)\\ &\quad + \omega^4\epsilon_t^2\left(-\omega_0^2 - 2\omega_0\omega_m - \omega_m^2 + \omega^2\right) = 0.\end{aligned} \tag{8}$$

Equations (7) and (8) are the LM and TM of the Weyl points. Based on Eq. (7), the angular frequency threshold of the GMs [Fig. 1(b)] is $\omega = \omega_p$. In the GMs, Eq. (8) can be solved to obtain the dispersion relation as

$$\begin{aligned}k_{z1}^{\pm} &= \pm\omega\frac{\sqrt{\epsilon_t(\omega_0 + \omega_m - \omega)}}{\sqrt{\omega_0 - \omega}},\\ k_{z2}^{\pm} &= \pm\omega\frac{\sqrt{\epsilon_t(\omega_0 + \omega_m + \omega)}}{\sqrt{\omega_0 + \omega}}.\end{aligned} \tag{9}$$

Equation (9) determines how many TMs can exist in the GM system along the z-axis direction under the specific angular frequency ω condition.

Along the y axis ($k_x = k_z = 0$), the characteristic equation [Eq. (6)] of the GMs can be further given by

$$-k_y^2 + \omega^2\epsilon_t = 0, \tag{10}$$

$$\begin{aligned}&\omega^2\left[\left(\omega_0^2 + 2\omega_0\omega_m + \omega_m^2 - \omega^2\right)\left(\omega_p^2 - \omega^2\right)\right.\\ &\quad\left. + \left(\omega_0^2 + \omega_0\omega_m - \omega^2\right)k_y^2\right]\epsilon_t = 0.\end{aligned} \tag{11}$$

Equations (10) and (11) represent the TM and LM of the nodal line. Equation (10) can then be solved to obtain the dispersion relation as $\pm k_y = \omega\sqrt{\epsilon_t}$; that is, under a specific angular frequency ω condition, only two k_y correspond to it. Then, based on Eqs. (10) and (11), the angular frequency

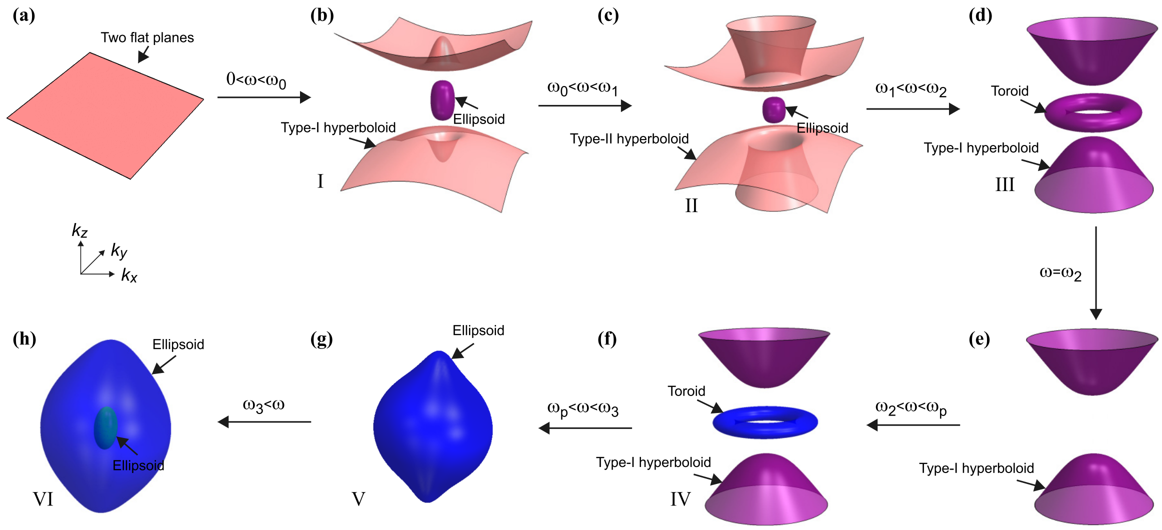

FIG. 2. Topological transitions of the GMs. (a) Highly anisotropic material when the angular frequency $\omega \to 0$. (g) The ellipsoidal equifrequency surface at the angular frequency $\omega = 2.7$. (b)–(f) and (h) The different types of equifrequency surfaces caused by the change of the angular frequency ω: (b) $\omega = 0.9$, (c) $\omega = 1.1$, (d) $\omega = 1.9$, (e) $\omega = 2.05$, (f) $\omega = 2.2$, and (h) $\omega = 3.2$, corresponding to phase I–VI regions in Fig. 1(b), respectively. The electromagnetic parameters of the GMs are $\epsilon_t = 2$, $\omega_0 = 1$, $\omega_m = 2$, and $\omega_p = 2.5$.

threshold of the GMs [Fig. 1(b)] is given by

$$\omega_2 = \frac{\sqrt{\omega_0^2 + 2\omega_0\omega_m + \omega_m^2 + \omega_p^2 - \omega_0^2\epsilon_t - \omega_0\omega_m\epsilon_t - k}}{\sqrt{2(1-\epsilon_t)}}, \tag{12}$$

where $k = \sqrt{4(\omega_0+\omega_m)^2\omega_p^2(-1+\epsilon_t) + [\omega_0^2 + 2\omega_0\omega_m + \omega_m^2 + \omega_p^2 - \omega_0(\omega_0+\omega_m)\epsilon_t]^2}$. In the GMs, the conditions for $\epsilon_t = 0$ and $\mathbf{k} = \mathbf{0}$ are $\omega_1 = \sqrt{\omega_0(\omega_0+\omega_m)}$ and $\omega_3 = \omega_0 + \omega_m$, respectively. Moreover, the resonance frequency $\omega_0(|\mu_t| = |g| \to \infty)$ exists in the GMs. Therefore, based on Eqs. (7) and (12), we demonstrate that the Weyl point and nodal line are the critical points in the topological transitions [Fig. 1(b)].

In the GMs, the dispersion characteristics of the electromagnetism components of Eq. (1) are shown in Fig. 1(b). Here, the phase diagram of different effective electromagnetic parameter combinations is distinguished by Roman numerals I–VI: in particular, $\epsilon_z < 0$ and $\mu_t > g > 0$ in region I; $\epsilon_z < 0$ and $g < \mu_t < 0$ in region II; $g < \epsilon_t < 0$ and $\mu_t > 0$ in regions III and IV; $\mu_t > \epsilon_z > 0$, $g < 0$, and $\mu_t < |g|$ in region V; and $\mu_t > \epsilon_z > 0$, $g < 0$, and $\mu_t > |g|$ in region VI.

In Figs. 1(c) and 1(d), based on Eqs. (7), (8), (10), and (11), we give the specific distribution of the TM and LM of the Weyl point and nodal line. In particular, the black lines and pink lines represent the TM and LM, respectively. The Weyl point [Eq. (7)] and nodal line [Eq. (11)] have flat or negative dispersion of the LM, respectively, as shown in Figs. 1(c) and 1(d). At the angular frequencies $\omega = \omega_p$ [Eq. (7)] and $\omega = \omega_2$ [Eq. (12)], we see the projection of the Weyl point and nodal line in the k_x-k_y plane, as depicted in Figs. 1(e) and 1(f). The Weyl point and nodal line have a 0D degenerate point [Fig. 1(e)] and 1D degenerate line [Fig. 1(f)] in their 3D band structures, respectively.

The topological characteristic of the Weyl points and nodal line in the GMs can be characterized by the nonzero topological charges (Chern numbers, C). Mathematically, the topological charges of the Weyl points and nodal line are described as the surface integral of the Berry curvature $[\Omega(\mathbf{k})]$ in momentum space at the angular frequencies $\omega = \omega_p$ and $\omega = \omega_2$: $C = \frac{1}{2\pi}\iint \mathbf{\Omega}(\mathbf{k}) \cdot d\mathbf{s} = \frac{1}{2\pi}\iint \nabla_{\mathbf{k}} \times \langle \mathbf{U}(\mathbf{k})|i\nabla_{\mathbf{k}}|\mathbf{U}(\mathbf{k})\rangle \cdot d\mathbf{s}$, where $\mathbf{U}(\mathbf{k}) = [\mathbf{E}, \mathbf{H}]^T$ represents the eigenpolarization mode of the GMs [1]. In particular, the Berry curvature of the Weyl points and the nodal line can be calculated at every point (k_y, k_z) on the 2D equifrequency surface of the GMs (the specific distributions of Berry curvature are given in Fig. 6 of the Appendix).

III. TOPOLOGICAL TRANSITIONS IN GMs

Based on the topological diagram in Fig. 1(b), we specifically give the distributions of equifrequency surfaces in the different regions [Fig. 1(b)]. In the GMs, there are different topology forms of the equifrequency surface because of the relation between the permittivity and permeability tensor components at different angular frequencies [Eq. (1)]. Therefore, the equifrequency surface can essentially vary by changing the angular frequency, as shown in Fig. 2. Moreover, the equifrequency surfaces of the GMs are symmetric about the x-y plane (Fig. 2).

If $\omega \to 0$, the electromagnetic parameter ϵ_z [Eq. (1)] approaches infinity. In this case, the radius of the equifrequency surfaces (pink plane) of the GMs is very large. Hence, the equifrequency surfaces are two flat planes in momentum

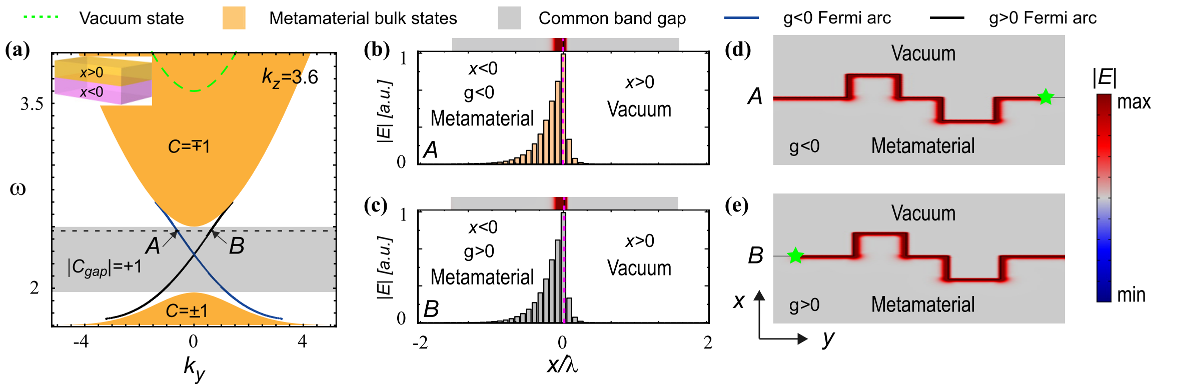

FIG. 3. Band structures, Fermi arc surface state, and topological surface wave. (a) Fermi arc surface states at the interface between the GMs and the vacuum state. The gray regions are the common band gaps in momentum space. (b) and (c) Mode profiles $|E|$ of the Fermi arc surface states of the points A and B in (a), respectively. The $x > 0$ and $x < 0$ regions represent the vacuum state and GMs, respectively. (d) and (e) Numerical simulations ($\omega = 2.48$) of propagation of the topological surface waves on the multiple step-type configurations, corresponding to A and B in (a), respectively. The green pentagrams present the electric dipoles. The electromagnetic parameters of the GMs are $k_z = 3.6$, $\epsilon_t = 2$, $\omega_0 = 1$, $|\omega_m| = 2$, and $\omega_p = 2.5$.

space, as illustrated in Fig. 2(a). In the phase I region of the topological diagram [Fig. 1(b)], the equifrequency surfaces (mixed-type dispersion) contain a twofold type-I hyperboloid (pink) and ellipsoid (orange) along the z axis of the GMs, as shown in Fig. 2(b). In the phase II region, the equifrequency surfaces of the twofold type-I hyperboloid in Fig. 2(b) become the twofold type-II hyperboloid form, as illustrated in Fig. 2(c). These two types of hyperboloids (type-I and type-II) in this paper are topologically nonequivalent because there is a hole in the type-II hyperbolic equifrequency surfaces that cannot be transformed into type-I through continuous deformation. Notably, the equifrequency surfaces (mixed-type dispersion) of the GMs are a twofold type-I hyperboloid (pink) and torus (pink) along the z axis in the phase III region, as shown in Fig. 2(d). The equifrequency surfaces are a twofold type-I hyperboloid (pink) because there are Weyl points ($\epsilon_z = 0$) along the z axis when $\omega = \omega_p$, as shown in Fig. 2(e).

In the phase IV region, similar to Fig. 2(d), the equifrequency surfaces return to the twofold type-I hyperboloid (pink) and torus (pink) form, as illustrated in Fig. 2(f). In the phase V region, $k_{z1}^{\pm}$ [Eq. (9)] represent the nonphysical solutions owing to $\omega_0 + \omega_p < \omega$. Therefore, only one ellipsoidal equifrequency surface exists in the GMs, as shown in Fig. 2(g). Moreover, there are two ellipsoid equifrequency surfaces (different radii) because of the time-reversal-symmetry breaking of the GMs, in the region VI [Fig. 2(h)]. Thus, by only changing the angular frequency ω in the GMs [Fig. 1(b)], the topological transitions can be realized; i.e., the equifrequency surfaces from a closed-form ellipsoid or torus change to the open-form type-I or type-II hyperboloid, as shown in Fig. 2.

IV. TOPOLOGICAL SURFACE WAVE AND TOPOLOGICAL BEAM SPLITTERS

Now, we study the Fermi arc surface states supported by the interface between the GMs and the vacuum state in the common band gap regions [gray shaded region in Fig. 3(a)]. We consider the 3D translation invariant in the y-z plane and stratified structures along the x axis, as shown in Fig. 3(a). The half-spaces $x > 0$ and $x < 0$ are occupied by the vacuum state and GMs, respectively. According to Maxwell equations, the eigenstates on each side of the interface ($x = 0$) can be obtained by the nontrivial solutions of the electric field **E** and magnetic field **H**.

In the vacuum state, the two independent eigenstates can be given by

$$\mathbf{E_1} = \left[-k_y k_{x1}, i\left(k_y^2 - \omega^2\right), ik_y k_z\right], \quad \mathbf{H_1} = (i\omega k_z, 0, \omega k_{x1}), \tag{13}$$

$$\mathbf{E_2} = \left[k_z k_{x1}, -ik_y k_z, i\left(-k_z^2 + \omega^2\right)\right], \quad \mathbf{H_2} = (i\omega k_y, \omega k_{x1}, 0), \tag{14}$$

where $k_{x1} = \sqrt{k_y^2 + k_z^2 - \omega^2}$ represents the attenuation constant inside the vacuum state. On the other hand, two independent eigenstates of the GMs can be described as

$$\mathbf{E}_3 = (E_{3x}, E_{3y}, E_{3z}), \mathbf{H}_3 = (H_{3x}, H_{3y}, H_{3z}), \tag{15}$$

$$\mathbf{E}_4 = (E_{4x}, E_{4y}, E_{4z}), \mathbf{H}_4 = (H_{4x}, H_{4y}, H_{4z}). \tag{16}$$

Then, applying Maxwell boundary conditions at $x = 0$ for the tangential magnetic fields and electric fields can lead to the 4×4 constraint matrix **M** determinant problem, i.e.,

$$\mathrm{Det}[\mathbf{M}] = \begin{vmatrix} E_{1y} & E_{2y} & E_{3y} & E_{4y} \\ E_{1z} & E_{2z} & E_{3z} & E_{4z} \\ H_{1y} & H_{2y} & H_{3y} & H_{4y} \\ H_{1z} & H_{2z} & H_{3z} & H_{4z} \end{vmatrix} = 0. \tag{17}$$

Equation (17) represents the characteristic equation of the Fermi arc surface states between the vacuum state and GMs [Fig. 3(a)].

Based on Eq. (17), we obtain the Fermi arc surface states between the vacuum state and GMs when $k_z = 3.6$, as shown by the blue and black lines in Fig. 3(a) (more distributions

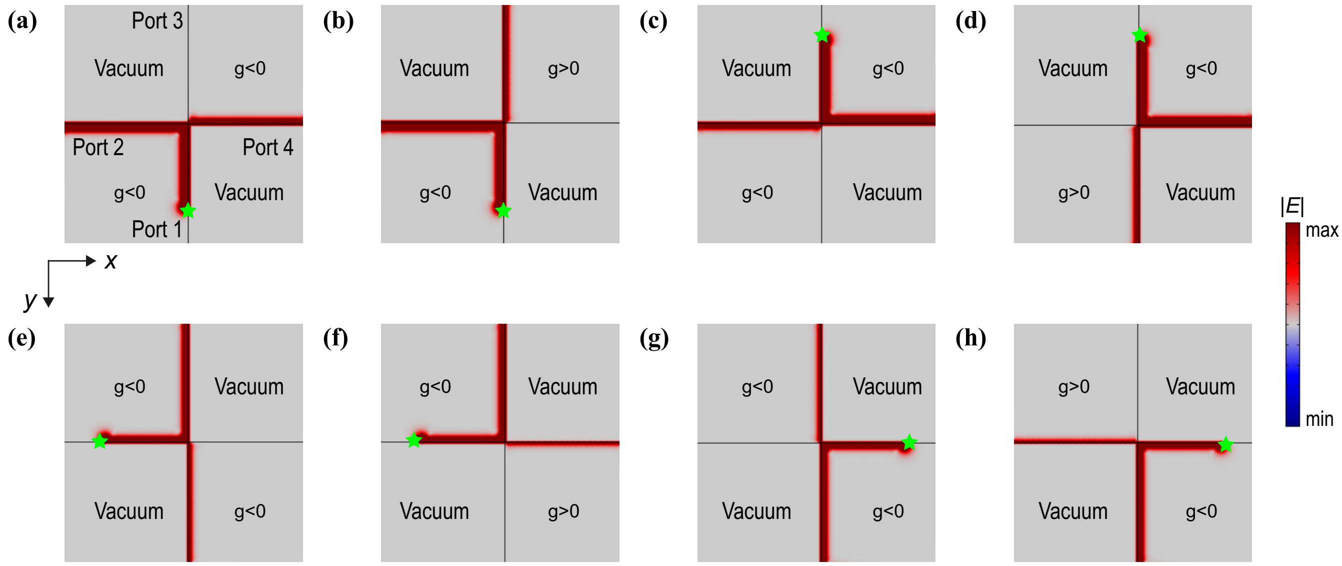

FIG. 4. Topological beam splitter by a cross waveguide (+ type). (a)–(h) The four-channel material system for the electromagnetic routine that consists of the vacuum state and GMs. The electromagnetic parameters of the GMs are the same as in Fig. 3.

of Fermi arc surface states at different frequencies ω are given in Fig. 7 of the Appendix). For the vacuum state–GMs system, the Fermi arc surface states are located in the common band gap region [Fig. 3(a)]. Therefore, these Fermi arc surface states possess local properties because there is no radiation mode entering the bulk states of the vacuum state and GMs. Moreover, we obtain the relative bandwidth α ($\alpha = 0.238388$) of the Fermi arc surface states [see the gray region in Fig. 3(a)]. The two different points A and B on the Fermi arc surface states both possess local characteristics, as shown in Figs. 3(b) and 3(c). The points A and B correspond to the Fermi arc surface states of the GMs with electromagnetic parameters $g < 0$ and $g > 0$ [Eq. (1)], respectively. For the vacuum state and GMs, the asymmetries of the one-dimensional electric field mode profile are caused by the different skin depths of the Fermi arc surface states in the two media, as illustrated in Figs. 3(b) and 3(c). Moreover, it should be noted that only the Fermi arc surface states in the common band gap regions [Fig. 3(a)] can be localized at the boundary. Otherwise, they will leak to the vacuum state and GMs. We give the time snapshots of the electric field $|E|$ (COMSOL Multiphysics) of the points A and B on the Fermi arc surface states [Fig. 3(a)], as shown in Figs. 3(d) and 3(e). In these numerical simulations (COMSOL 2D frequency domain), an electric dipole can be used as the source located on the interface between the vacuum state and GMs. The surface wave in Figs. 3(d) and 3(e) can transmit without any reflection against the multiple step-type structural defects. It can directly demonstrate the topological characteristics of the GMs system from the physical phenomenon level. Moreover, by flipping the gyromagnetic parameters g of the GMs, the transmission direction of the surface waves between the vacuum state and GMs can be reversed, as shown in Figs. 3(d) and 3(e). The physical mechanism of achieving the reversal of propagation direction of the surface wave is caused by opposite gap Chern numbers [$C_{\text{gap}} = +1(C_{\text{gap}} = +1)$] of the vacuum state–GMs system, as illustrated in Fig. 3(a).

The topological Fermi arc surface states discussed in Figs. 3(a) and 7 can be useful for designing functional topological devices based on the GMs. We built the four-channel vacuum state–GMs system that contains two types (+ type and M type) of electromagnetic routing channels, as shown in Figs. 4 and 5. The topological surface waves can bypass sharp defects and output signals at different ports to achieve topological beam splitting. The physical mechanism of achieving the topological beam splitters is caused by different group velocity directions of the Fermi arcs surface states of the vacuum state–GMs system (see Fig. 8).

Now, we will study the topological beam splitters in the vacuum state–GMs system. Here, we take Fig. 4(a) as an example to specifically analyze topological beam splitting in the materials system. According to the bulk-edge correspondence, the half-spaces $x > 0$ and $x < 0$ are occupied by the GMs with $g < 0$ (vacuum state) and vacuum state (GMs with $g > 0$); there are Fermi arc surface states propagating in the positive and negative directions along the y axis, respectively (see details in Fig. 8 of the Appendix). In particular, when the Fermi arc surface states are excited from port 1, the surface wave will couple to the Fermi arc surface state of the half-spaces $x > 0$ and $x < 0$ that are occupied by the vacuum state and GMs with $g > 0$ along the negative y-axis direction, and then transmit along the negative y-axis direction, as illustrated in Fig. 4(a). However, port 3 has no surface wave output because there is no Fermi arc surface state along the negative y direction of the half-spaces $x > 0$ and $x < 0$ that are occupied by the GMs with $g < 0$ and vacuum state. Thus, the topological surface waves are only output at ports 2 and 4 to achieve a controllable transmission direction of surface wave topological beam splitting effect at the output port, as shown in Fig. 4(a). Moreover, the topological beam splitters can be realized direction (shape) reconfigurable by manipulating the locations of the vacuum state and GMs (+ type and M type form electromagnetic routing channels), as illustrated in Figs. 4 and 5.

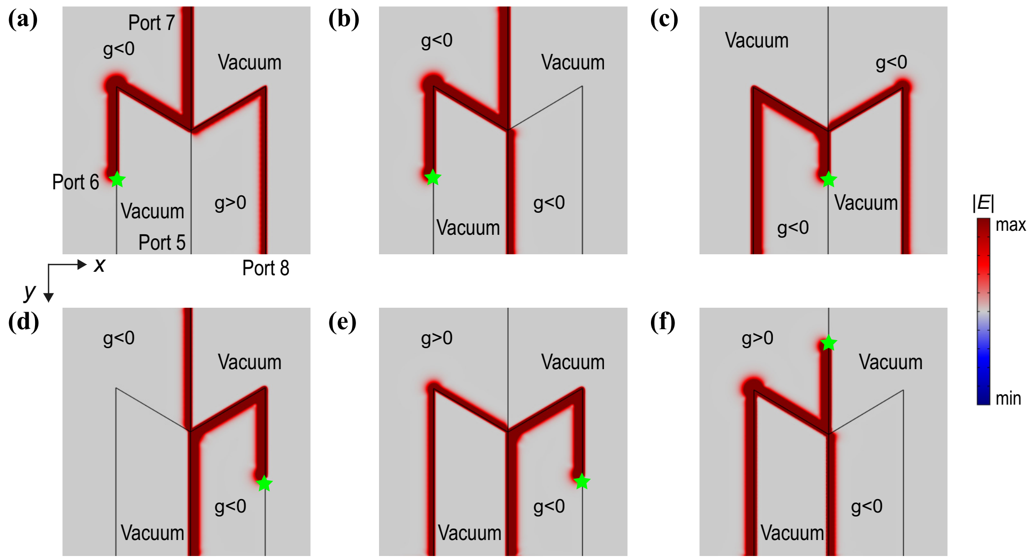

FIG. 5. M-type topological beam splitter. (a)–(f) The four-channel material system for the electromagnetic routine that consists of the vacuum state and GMs. The electromagnetic parameters of the GMs are the same as in Fig. 3.

V. CONCLUSIONS

In conclusion, we study the topological transitions and realize the topological beam splitters in the GMs. By solving the bulk state equation of the GMs, we analytically calculated the conditions for the critical points of topological transitions and comprehensively drew the topological phase diagrams in the GMs. To demonstrate the existence of the Weyl point and nodal line in the GMs and prove its related physical properties, we specifically deduced the equations of the TM and LM based on the eigen-electric-field that forms the Weyl point and nodal line of the GMs. Remarkably, it is demonstrated that the Weyl point and nodal line coexist in the GMs. This nodal line and the Weyl points are the critical points in the topological transitions and have the spatial inversion symmetry protection mechanism. According to the bulk-edge correspondence, the localized Fermi arc surface states can exist at the interface between the vacuum state and GMs. The numerical simulation results demonstrate that the surface waves at the boundary between the GMs and vacuum state can propagate robustly against the multiple-step transition. Based on the topological surface waves, we realize the topological beam splitters between the GMs and the vacuum state. We reveal that the physical mechanism of achieving the topological beam splitters is caused by the different group velocity directions of the Fermi arcs surface states of the GMs–vacuum state system. Notably, the topological beam splitters based on the Fermi arc surface states in the topological GMs can achieve robustness features to structural perturbations and defects, achieving a controllable propagation direction topological optical beam effect in the GMs. Moreover, the topological beam splitters can be realized direction reconfigurable by manipulating the locations of the vacuum state and GMs. We believe our work may provide new insights into the topological wave physics in the homogeneous media without any periodicity restrictions, which may help achieve the topological optical devices in practice.

ACKNOWLEDGMENT

This work was supported by the National Natural Science Foundation of China (NSFC) (Grants No. 12304472, No. 12304557, No. 12074094, No. 11874132, and No. 61575055).

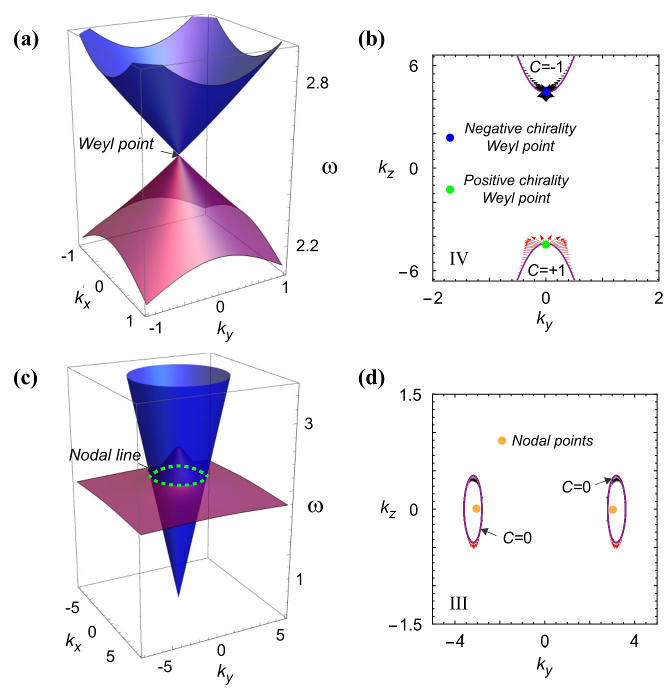

FIG. 6. Weyl point, nodal line, and topological charges. (a) and (c) The 3D band dispersion of the Weyl point and nodal line in the k_x-k_y-ω space, respectively. (b) and (d) Berry curvatures and topological charges of the 2D equifrequency surfaces for the GMs with $k_x = 0$. The electromagnetic parameters of the GMs are the same as in Fig. 1.

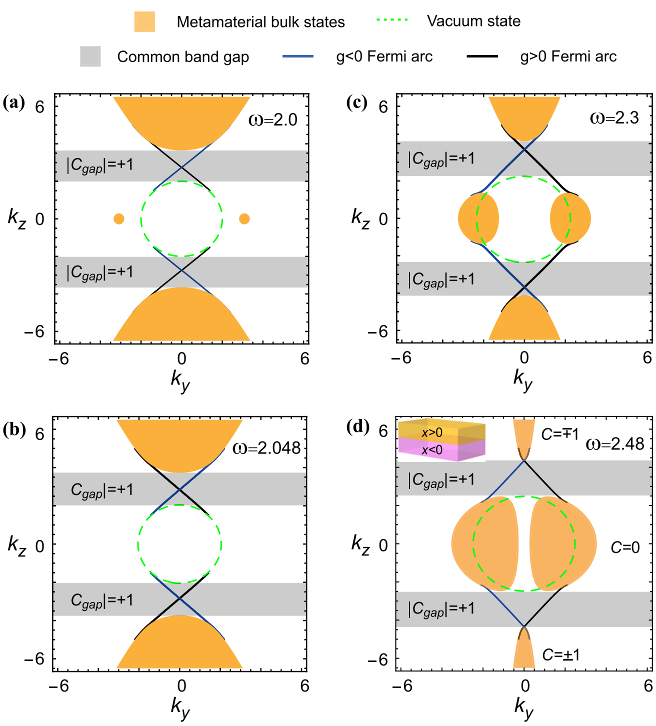

FIG. 7. (a)–(d) Equifrequency surfaces of GMs and Fermi arc surface states at different frequencies ω.

APPENDIX

To clearly distinguish between the Weyl point and nodal line band structure degenerate dimensional, the 3D (k_x-k_y-ω) band structures of these nodal points (Weyl point and nodal line) are given in Figs. 6(a) and 6(c), respectively. According to Eqs. (7) and (12), it can be obtained that the Weyl point and nodal line in GMs are located at different angular frequencies $\omega_p = 2.5$ [see Eq. (7)] and $\omega_2 = 2.04607$ [see Eq. (12)], respectively. Therefore, the band dispersion characteristics near the Weyl point and nodal line are analyzed with $\omega_p = 2.5$ and $\omega_2 = 2.04607$ as the center frequencies in Figs. 6(a) and 6(c), respectively.

In Figs. 6(b) and 6(d), the red and black arrows represent the outward and inward Berry curvatures, respectively. The length of the red (black) arrows represents the amplitudes of the Berry curvatures. For the Weyl points, the Berry curvatures of each of its equifrequency surfaces diverge (converges) in the same direction [see Fig. 6(b)]. However, the nodal line has an equal amount of opposite divergence (convergence) Berry curvature for each of its equifrequency surfaces [see Fig. 6(d)]. Furthermore, we can obtain the Chern number corresponding to the equifrequency surface of the GMs by composing the area of the Berry curvature on the entire surface. Thus, the Weyl points and nodal line have the net nonzero topological charge ($|C| = 1$) and zero topological charge ($|C| = 0$), respectively.

In the the GMs ($g > 0$ or $g < 0$)–vacuum system, the difference of the topological invariants of the common band gap remains constant ($|C_{\text{gap}}| = 1$), so the number of Fermi arc surface states in the band gap is constant and independent of frequency ω, as shown in the Fig. 7. Notably, the middle bulk states of GMs in Figs. 7(a)–7(d) undergo significant changes at different frequencies ω, with two closed rings undergoing a process of disappearance [see Fig. 7(b)] and reproduction [see Figs. 7(c) and 7(d)]. However, the number of the Fermi arc surface states in the common band gap (gray regions) does not change because of the gap Chern number $|C_{\text{gap}}| = 1$ in Fig. 7.

We take Fig. 4(a) as an example to illustrate that the output signal in the topology beam splitter is output from two ports. As shown in Fig. 8(a), in the x-y plane (fixed $k_z = 3.6$), the topological surface wave of interface I only transmits along the negative y axis, and the wave vector of the traveling wave in the x direction is zero [see Fig. 8(b)].

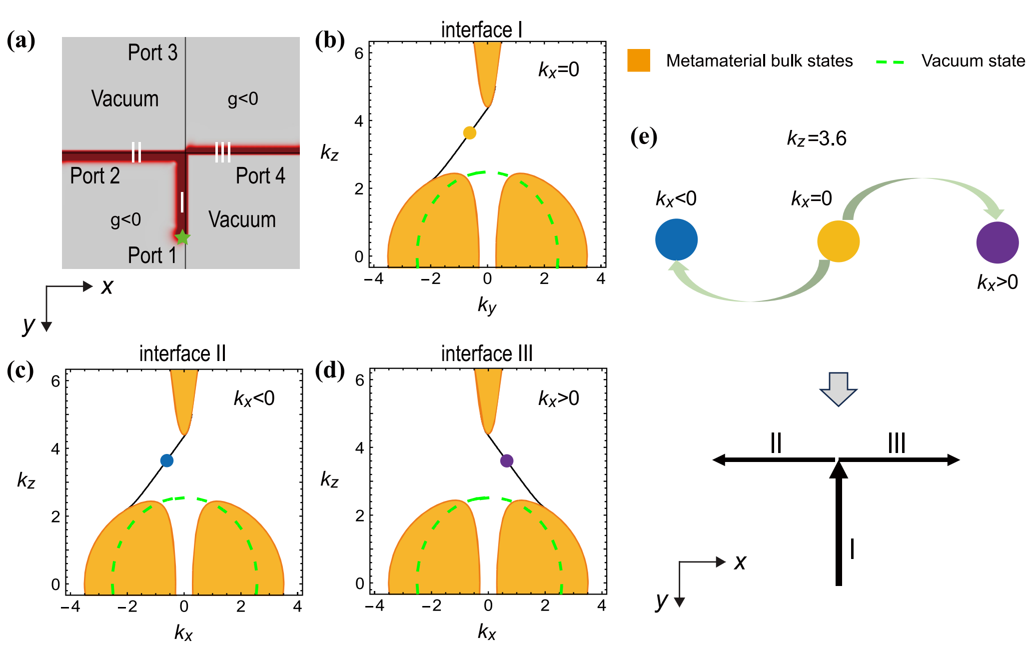

FIG. 8. Dispersion relation and symmetry analysis of the topological beam splitter.

However, at interfaces II and III, surface waves propagate in the negative ($k_x < 0$) and positive ($k_x > 0$) directions along the x axis [see Figs. 8(c) and 8(d)], respectively. In addition, the only difference between the II and III interfaces is the reversal of the spatial positions of vacuum and GMs. In terms of symmetry, the Fermi arc surface state at the II interface can be equivalently regarded as the "time-reversal symmetry mode" at the III interface. Therefore, when the surface wave of interface I passes through the intersection point, this mode is coupled to the Fermi arc of interfaces II and III, and theoretically, the efficiency of coupling to the two interfaces is equal, as shown by the black arrows in Fig. 8(e).

[1] L. Lu, J. D. Joannopoulos, and M. Soljačić, Topological photonics, Nat. Photon. **8**, 821 (2014).

[2] A. B. Khanikaev and G. Shvets, Two-dimensional topological photonics, Nat. Photon. **11**, 763 (2017).

[3] T. Ozawa, H. M. Price, A. Amo, N. Goldman, M. Hafezi, L. Lu, M. C. Rechtsman, D. Schuster, J. Simon, O. Zilberberg, and I. Carusotto, Topological photonics, Rev. Mod. Phys. **91**, 015006 (2019).

[4] M. Kim, Z. Jacob, and J. Rho, Recent advances in 2D, 3D and higher-order topological photonics, Light Sci. Appl. **9**, 130 (2020).

[5] H. Xue, Y. Yang, and B. Zhang, Topological acoustics, Nat. Rev. Mater. **7**, 974 (2022).

[6] X. Zhang, F. Zangeneh-Nejad, Z. Chen, M. Lu, and J. Christensen, A second wave of topological phenomena in photonics and acoustics, Nature (London) **618**, 687 (2023).

[7] N. Han, X. Xi, Y. Meng, H. Chen, Z. Gao, and Y. Yang, Topological photonics in three and higher dimensions, APL Photon. **9**, 010902 (2024).

[8] S. Ali Hassani Gangaraj and F. Monticone, Physical violations of the bulk-edge correspondence in topological electromagnetics, Phys. Rev. Lett. **124**, 153901 (2020).

[9] Y. Fu and H. Qin, Topological phases and bulk-edge correspondence of magnetized cold plasmas, Nat. Commun. **12**, 3924 (2021).

[10] N. Han, J. Liu, Y. Gao, K. Zhou, and S. Liu, Anomalous bulk-edge correspondence and dual-band topologically protected edge states in magnetized plasma, Phys. Rev. B **105**, 235411 (2022).

[11] G. G. Liu, Z. Gao, Q. Wang, X. Xi, Y. H. Hu, M. Wang, C. Liu, X. Lin, L. Deng, S. A. Yang, P. Zhou, Y. Yang, Y. Chong, and B. Zhang, Topological Chern vectors in three-dimensional photonic crystals, Nature (London) **609**, 925 (2022).

[12] H. Jia, R. Zhang, W. Gao, Q. Guo, B. Yang, J. Hu, Y. Bi, Y. Xiang, C. Liu, and S. Zhang, Observation of chiral zero mode in inhomogeneous three-dimensional Weyl metamaterials, Science **363**, 148 (2019).

[13] S. Ma, H. Jia, Y. Bi, S. Ning, F. Guan, H. Liu, C. Wang, and S. Zhang, Gauge field induced chiral zero mode in five-dimensional Yang monopole metamaterials, Phys. Rev. Lett. **130**, 243801 (2023).

[14] B. Yang, Q. Guo, D. Wang, H. Wang, L. Xia, W. Xu, M. Kang, R. Zhang, Z. Zhang, Z. Zhu, and C. T. Chan, Scalar topological photonic nested meta-crystals and skyrmion surface states in the light cone continuum, Nat. Mater. **22**, 1203 (2023).

[15] J. Noh, S. Huang, D. Leykam, Y. D. Chong, K. P. Chen, and M. C. Rechtsman, Experimental observation of optical Weyl points and Fermi arc-like surface states, Nat. Phys. **13**, 611 (2017).

[16] S. Vaidya, J. Noh, A. Cerjan, C. Jörg, G. Von Freymann, and M. C. Rechtsman, Observation of a charge-2 photonic Weyl point in the infrared, Phys. Rev. Lett. **125**, 253902 (2020).

[17] B. Xie, H. Liu, H. Wang, H. Cheng, J. Tian, and S. Chen, A review of topological semimetal phases in photonic artificial microstructures, Front. Phys. **9**, 771481 (2021).

[18] Z. Lan, M. L. N. Chen, F. Gao, S. Zhang, and E. I. Wei, A brief review of topological photonics in one, two, and three dimensions, Rev. Phys. **9**, 100076 (2022).

[19] M. Li, N. Han, L. Peng, and S. Zhang, Type-II Dirac points and topological Fermi arcs in nonlocal metamaterials, Phys. Rev. B **106**, 235303 (2022).

[20] Q. Yan, R. Liu, Z. Yan, B. Liu, H. Chen, Z. Wang, and L. Lu, Experimental discovery of nodal chains, Nat. Phys. **14**, 461 (2018).

[21] A. Cerjan, S. Huang, M. Wang, K. P. Chen, Y. Chong, and M. C. Rechtsman, Experimental realization of a Weyl exceptional ring, Nat. Photon. **13**, 623 (2019).

[22] H. Park, W. Gao, X. Zhang, and S. S. Oh. Nodal lines in momentum space: Topological invariants and recent realizations in photonic and other systems, Nanophotonics **11**, 2779 (2022).

[23] J. W. Liu, F. L. Shi, K. Shen, X. D. Chen, K. Chen, W. J. Chen, and J. W. Dong, Antichiral surface states in time-reversal-invariant photonic semimetals, Nat. Commun. **14**, 2027 (2023).

[24] Y. Yang, J. Xia, H. Sun, Y. Ge, D. Jia, S. Yuan, S. A. Yang, Y. Chong, and B. Zhang, Observation of a topological nodal surface and its surface-state arcs in an artificial acoustic crystal, Nat. Commun. **10**, 5185 (2019).

[25] M. Kim, D. Lee, D. Lee, and J. Rho, Topologically nontrivial photonic nodal surface in a photonic metamaterial, Phys. Rev. B **99**, 235423 (2019).

[26] H. He, C. Qiu, L. Ye, X. Cai, X. Fan, M. Ke, F. Zhang, and Z. Liu, Topological negative refraction of surface acoustic waves in a Weyl phononic crystal, Nature (London) **560**, 61 (2018).

[27] Y. Yang, H. Sun, J. Xia, H. Xue, Z. Gao, Y. Ge, D. Jia, S. Yuan, Y. Chong, and B. Zhang, Topological triply degenerate point with double Fermi arcs, Nat. Phys. **15**, 645 (2019).

[28] M. Li, N. Han, J. Song, and Y. Jiang, Unidirectional disorder-immune transmission and reconfigurable route of Fermi arcs in photonic topological Weyl metamaterials, Phys. Rev. B **106**, 075301 (2022).

[29] X. Xi, B. Yan, L. Yang, Y. Meng, Z. X. Zhu, J. M. Chen, Z. Wang, P. Zhou, P. Shum, Y. Yang, H. Chen, S. Mandal, G. Liu, B. Zhang, and Z. Gao, Topological antichiral surface states in a magnetic Weyl photonic crystal, Nat. Commun. **14**, 1991 (2023).

[30] M. Li, N. Han, L. Qi, Z. Lin, S. Cui, G. Chen, and L. Peng, Fermi arc surface state and topological switch in the gyromagnetic metamaterials, New J. Phys. **25**, 053026 (2023).

[31] Q. Guo, O. You, B. Yang, J. B. Sellman, E. Blythe, H. Liu, Y. Xiang, J. Li, J. Li, D. Fan, J. Chen, C. T. Chan, and S. Zhang, Observation of three-dimensional photonic Dirac points and spin-polarized surface arcs, Phys. Rev. Lett. **122**, 203903 (2019).

[32] S. Ma, B. Yang, and S. Zhang, Topological photonics in metamaterials, Photon. Insights **1**, R02 (2022).

[33] Q. Guo, W. Gao, J. Chen, Y. Liu, and S. Zhang, Line degeneracy and strong spin-orbit coupling of light with bulk bianisotropic metamaterials, Phys. Rev. Lett. **115**, 067402 (2015).

[34] H. N. Krishnamoorthy, Z. Jacob, E. Narimanov, I. Kretzschmar, and V. M. Menon, Topological transitions in metamaterials, Science **336**, 205 (2012).

[35] P. N. Dyachenko, S. Molesky, A. Y. Petrov, M. Stormer, T. Krekeler, S. Lang, M. Ritter, Z. Jacob, and M. Eich, Controlling thermal emission with refractory epsilon-near-zero metamaterials via topological transitions, Nat. Commun. **7**, 11809 (2016).

[36] V. I. Fesenko and V. R. Tuz, Lossless and loss-induced topological transitions of isofrequency surface in a biaxial gyroeletromagnetic medium, Phys. Rev. B **99**, 094404 (2019).

[37] Y. Gelkop, F. D. Mei, S. Frishman, Y. Garcia, L. Falsi, G. Perepelitsa, C. Conti, E. DelRe, and A. J. Agranat, Hyperbolic optics and superlensing in room-temperature KTN from self-induced k-space topological transitions, Nat. Commun. **12**, 7241 (2021).

[38] Y. Chen, X. He, Y. Cheng, H. Qiu, L. Feng, M. Zhang, D. Dai, G. Guo, J. Dong, and X. Ren, Topologically protected valley-dependent quantum photonic circuits, Phys. Rev. Lett. **126**, 230503 (2021).

[39] X. Zhang, F. Yu, Z. Chen, Z. Tian, Q. Chen, H. Sun, and G. Ma, Non-Abelian braiding on photonic chips, Nat. Photon. **16**, 390 (2022).

[40] Q. Zhang, D. Lee, L. Zheng, X. Ma, S. I. Meyer, L. He, H. Ye, Z. Gong, B. Zhen, K. Lai, and A. T. C. Johnson, Gigahertz topological valley Hall effect in nanoelectromechanical phononic crystals, Nat. Electron. **5**, 157 (2022).

[41] S. Wang, C. Qin, L. Zhao, H. Ye, S. Longhi, P. Lu, and B. Wang, Photonic Floquet Landau-Zener tunneling and temporal beam splitters, Sci. Adv. **9**, eadh0415 (2023).

[42] J. Hou, Z. Li, X. Luo, Q. Gu, and C. Zhang, Topological bands and triply degenerate points in non-Hermitian hyperbolic metamaterials, Phys. Rev. Lett. **124**, 073603 (2020).

[43] M. Li, J. Song, and Y. Jiang, Photonic topological Weyl degeneracies and ideal type-I Weyl points in the gyromagnetic metamaterials, Phys. Rev. B **103**, 045307 (2021).

[44] A. M. Holmes, M. Sabbaghi, and G. W. Hanson, Experimental realization of topologically protected unidirectional surface magnon polaritons on ceramic YIG ferrites, Phys. Rev. B **104**, 214433 (2021).

[45] W. Yang, Q. Liu, H. Wang, Y. Chen, R. Yang, S. Xia, Y. Luo, L. Deng, J. Qin, H. Duan, and L. Bi, Observation of optical gyromagnetic properties in a magneto-plasmonic metamaterial, Nat. Commun. **13**, 1719 (2022).

[46] B. Wood, J. B. Pendry, and D. P. Tsai, Directed subwavelength imaging using a layered metal-dielectric system, Phys. Rev. B **74**, 115116 (2006).

[47] N. Han, J. L. Liu, Y. Gao, K. Y. Zhou, and S. T. Liu, Topologically protected and highly localized surface waves in gyro-electromagnetic metamaterials, Ann. Phys. (Berlin) **532**, 2000022 (2020).